

Electrically charged magnetic skyrmions

O. G. Udalov^{1,2} and I. S. Beloborodov¹

¹*Department of Physics and Astronomy, California State University Northridge, Northridge, California 91330, USA*

²*Institute for Physics of Microstructures RAS, Nizhny Novgorod 603950, Russia*

 (Received 7 June 2022; revised 4 August 2022; accepted 12 September 2022; published 19 September 2022)

We consider magnetic oxide/heavy metal oxide hybrid film on top of a substrate with high dielectric constant. We use the double exchange model to describe the system behavior. The interface between two oxide films produces Rashba spin-orbit interaction. The phase separation appears in such a magnetic film. Combination of the phase separation and spin-orbit coupling leads to formation of electrically charged magnetic clusters with skyrmions. We show that such clusters have both electrical and topological charges. Importantly, clusters with sizes suitable for skyrmions formation may occur only for substrate with a high dielectric constant.

DOI: [10.1103/PhysRevB.106.104423](https://doi.org/10.1103/PhysRevB.106.104423)

I. INTRODUCTION

Interfaces between ferromagnetic metals and heavy metals attract a lot of attention since they produce strong Dzyaloshinskii-Moriya interaction (DMI) stabilizing magnetic skyrmions in such hybrid films [1–4]. In the last decade transitional metal/heavy metal systems (such as Co/Pt) were studied a lot [5–9]. Recently, hybrid magnetic oxide (MO) films came into focus for many groups [10–24]. It was found that such multilayer structures can also produce strong enough DMI interaction and even host magnetic skyrmions (Sks).

Even a single magnetic oxide film shows a very rich physics. There are plenty of magnetic states that can be realized in such a film [checkerboard antiferromagnetic (AFM) state, canted AFM state, layered AFM state, and ferromagnetic (FM) state] depending on the doping or other conditions [25–28]. Electron transport also shows nontrivial behavior. Magnetic oxides are famous for the metal-insulator transition caused by the external magnetic field [29–31].

One of the interesting phenomena occurring in MO materials is the so-called phase separation [32–37]. In a phase separated state the current carriers are gathered in clusters with FM ordering. These clusters are surrounded by AFM insulating regions with no charge carrier.

The rich physics of magnetic oxides appears due to many-body effects, essential contribution of the Coulomb interaction, and competing types of exchange interaction. One of the simplest models describing magnetic oxides is the double exchange model with conduction electrons and localized magnetic moments interacting through an exchange interaction [26,32]. Short-range Coulomb interaction is often taken into account via on-site repulsion of conduction electrons [28,38,39]. Long-range interaction (important in the phase separated state) is considered when long-range charge inhomogeneities occur in magnetic oxides [40–43].

Recently, the model of the MO was extended by including the Rashba spin-orbit interaction (SOI) occurring at an interface between MO and another layer [16,44–46]. Such a Rashba interaction leads to the appearance of an effective DMI. Mostly, the case of high electron concentration was

considered. Electron density in this case does not have any long-range inhomogeneities. It was shown that Sks (and Sk lattices) may be stable in such magnetic films. Experimental studies confirm the theoretical predictions.

While the case of high electron density is interesting due to many-body correlation effects, the opposite case of low concentration provides other intriguing opportunities. In particular, in the system with low electron concentration, the phase separation may occur. Recently, it was shown that MO in a phase separated state shows unusual magnetoelectric coupling phenomena due to the interplay between phase separation and the Coulomb interaction screening effects [42,43]. In the present work we consider the model of the MO with Rashba SOI and low electron concentration where the phase separation occurs. The system is shown in Fig. 1. We assume that there is a bilayer film consisting of magnetic oxide and another oxide layer. The system is placed on top of the sub-

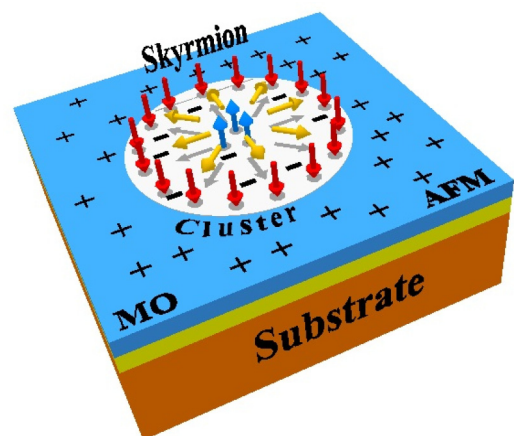


FIG. 1. Bilayer magnetic oxide film on top of a substrate. Due to the phase separation negatively charged clusters (only one is shown) appear. Outside of the clusters (blue region) the magnetic state is AFM. This region is positively charged. Inside of the cluster a magnetic skyrmion appears.

strate with a high dielectric constant. We show that due to the combination of the phase separation and the SOI, electrically charged clusters with nonzero topological magnetic charge may occur. Such a situation is shown in Fig. 1. A conductive cluster with an excessive amount of electrons (gray circle) is surrounded by an insulating region (blue). The insulating region has AFM state, while the cluster hosts a magnetic skyrmion.

The paper is organized as follows. The main idea and model are discussed in Sec. II. In Sec. III we consider possible magnetic states of the MO hybrid film and discuss the appearance of the electrically and topologically charged clusters. Finally, we define the parameters region where such clusters appear.

II. MAIN IDEA AND MODEL

Here we consider the magnetic oxide film with strong Rashba SOI occurring at the interface between magnetic oxide and the substrate or other nonmagnetic layer. We answer the question if the phase separation can appear in this system and if a skyrmion can occur in magnetic clusters in the phase separated state. It is known that under certain conditions electrons can gather in small clusters in the MO film. A FM state appears inside of these clusters due to increased electron density favoring the FM exchange interaction. Outside of these clusters, electrons are absent and the AFM state is realized due to AFM direct exchange between localized magnetic moments. The Rashba SOI of electrons effectively leads to the DMI interaction between localized magnetic moments. The DMI interaction may form a Sk in the FM cluster. Since electrons gather together in the clusters the electric charge occurs. Finally, we have electrically and topologically charged clusters in the AFM insulating matrix. Here we will check if such a state is possible.

A. Hamiltonian of the system

We consider a bilayer MO film consisting of a magnetic and a nonmagnetic layer. The magnetic layer has the thickness t . The film is in (x, y) plane. The bilayer system is placed on top of a substrate with a dielectric constant ϵ . There are localized magnetic moments and conduction electrons in the magnetic film. The Hamiltonian of the system has magnetic and electronic parts

$$H_{\text{tot}} = H_{\text{mag}} + H_{\text{el}}. \quad (1)$$

The localized magnetic moments form magnetization of the sample. The magnetic moments are treated as classical vectors using an effective Hamiltonian

$$H_{\text{mag}} = H_{\text{ex}} + H_{\text{an}} + H_{\text{ms}}, \quad (2)$$

with the exchange interaction H_{ex} , anisotropy H_{an} , and dipole-dipole interaction H_{ms} . We consider the nearest neighbor exchange interaction $-J(\mathbf{m}_i \mathbf{m}_j)$, where \mathbf{m}_i is the unit vector co-directed with magnetic moment i . The ion magnetic moment magnitude is m_s . The exchange interaction between localized magnetic moments is AFM ($J < 0$). The magnetic anisotropy is out-of-plane. It may appear due to the interfacial effects. We assume that all magnetic moments experience the

same anisotropy described by the term $-K m_z^2/2$. The long-range magnetodipole interaction has the form

$$H_{\text{ms}} = \sum_{i,j} [(\mathbf{m}_i \mathbf{m}_j) - 3(\mathbf{m}_i \mathbf{r}_{ij})(\mathbf{m}_j \mathbf{r}_{ij})]/r_{ij}^5, \quad (3)$$

where \mathbf{r}_{ij} is the vector connecting two ions.

We consider the magnetic material with cubic lattice with the lattice constant Δ . Besides the localized magnetic moments there are conduction electrons in the system. The average electron density is n_0 . Note that near the interface there could be an embedded electric field influencing the electron density. We assume that n_0 is the density taking this effect into account.

Delocalized electrons have a few contributions to energy. A kinetic energy (E_{kin}) is obtained within a tight-binding model with hopping matrix element t_0 . There is an s - d interaction (with characteristic energy J_{sd}) between electrons and localized magnetic moments. Due to the s - d interaction the hopping matrix element is renormalized $t_0 \rightarrow t_0 \cos(\theta/2)$, where θ is the angle between localized magnetic moments of neighboring sites. An electron momentum \mathbf{p} can be introduced in the tight-binding model.

There is a Rashba SOI, which may occur due to the interface between the MO film and another layer or substrate. A single electron SOI Hamiltonian has the form

$$H_{\text{so}} = -\alpha_{\text{so}}(\boldsymbol{\sigma} \cdot [\mathbf{z}_0 \times \mathbf{p}]) = \alpha_{\text{so}} \begin{pmatrix} 0 & p_y + ip_x \\ p_y - ip_x & 0 \end{pmatrix}, \quad (4)$$

where α_{so} is the spin-orbit coupling constant, \mathbf{p} is the momentum operator, and \mathbf{z}_0 is the normal to the film.

In a phase separated state the electron density becomes inhomogeneous and the long-range Coulomb interaction (H_C) contributes to the system energy. The total electron Hamiltonian has the form

$$H_{\text{el}} = H_{\text{kin}} + H_{\text{so}} + H_C. \quad (5)$$

We will discuss the Coulomb energy H_C in the next section for each particular magnetic state of the film.

B. Magnetization distribution of a skyrmion

Below we consider several different magnetic states. One of them is a skyrmion state. It is a cylindrically symmetric magnetization distribution with magnetization given by

$$\mathbf{m} = [m_{\perp}(\rho) \cos(\varphi + \varphi_0), m_{\perp}(\rho) \sin(\varphi + \varphi_0), m_z(\rho)], \quad (6)$$

where $m_z^2 + m_{\perp}^2 = 1$. Such a distribution can describe a Sk with a different domain wall (WD) type (“Néel” $\varphi_0 = 0$ and “Bloch” $\varphi_0 = \pi/2$). A Sk radius r_{sk} can be introduced. In the Sk center ($\rho < r_{\text{sk}}$) $m_{\perp} \approx 0$ and $m_z \approx 1$. In the external region of the skyrmion ($\rho > r_{\text{sk}}$) the z component of magnetization is negative $m_z \approx -1$ and $m_{\perp} \approx 0$. Near the Sk radius ($\rho \approx r_{\text{sk}}$) the transition region (domain wall) appears where m_z changes the sign and m_{\perp} becomes large. The transition region width is w_{dw} .

C. Effective DMI interaction

For the case of Sk magnetization distribution, the contribution of the Rashba SOI is nonzero. The electron’s SOI can

be transformed to an effective DMI of the localized magnetic moments. To estimate the effective DMI we use the following assumptions. First, we consider the limit of low electron concentration and replace the tight-binding model with a free-electron model with an effective mass. The effective single electron Hamiltonian has the form

$$H_{\text{el}} = \mathbf{p}^2/2m_e + H_{\text{so}}, \quad (7)$$

where m_e is the effective electron mass. It is related to the hopping matrix element as $m_e = \hbar^2/t_0/\Delta^2$, where Δ is the lattice constant. We assume here that the localized magnetic moment orientation changes slowly in space, and corrections to the effective mass due to the magnetic moment noncollinearity can be neglected. The single electron SOI energy can be rewritten in the cylindrical coordinates (ρ and ϕ) as follows:

$$H_{\text{so}} = \alpha_{\text{so}} \begin{pmatrix} 0 & e^{-i\phi}(p_\phi + ip_\rho) \\ e^{i\phi}(p_\phi - ip_\rho) & 0 \end{pmatrix}, \quad (8)$$

where $p_\phi = -i\hbar/\rho\partial_\phi$ and $p_\rho = -i\hbar\partial_\rho$. We denote the off-diagonal parts of the SOI operator as H_{so}^+ (upper right) and H_{so}^- (lower left).

We consider the case when characteristic skyrmion size is much bigger than the electron wavelength λ_F and the momentum conservation length λ_p . In this limit we can treat the skyrmion as a slowly spatially varying magnetization distribution. Also, we consider the case of strong s - d interaction and use the adiabatic approximation [$(\hbar k_F q/m_e)/(J_{sd}/\hbar) \ll 1$, where $q \sim |\partial\mathbf{m}/\partial\mathbf{r}|$] [47]. In this approximation, an electron magnetic moment follows the magnetization of the skyrmion. In the quadiabatic approximation, electron wave functions have the form

$$\Psi = \psi_s \psi_k = \begin{pmatrix} \Psi_\uparrow e^{-i\phi/2} \\ \Psi_\downarrow e^{i\phi/2} \end{pmatrix} e^{i(\mathbf{k}\mathbf{r})}, \quad (9)$$

where ψ_s is the spin-dependent part and $\psi_k = e^{i\mathbf{k}\mathbf{r}}$. Note that the spin-dependent part does not depend on \mathbf{k} and is the same for all electrons with the same spin projection. Such a wave function produces a vortexlike rotation (with winding number +1) of the electron spin (σ) when one goes around the coordinates origin:

$$\begin{aligned} \langle \sigma_x \rangle &= \text{Re}(\Psi_\uparrow^* \Psi_\downarrow) \cos(\phi) - \text{Im}(\Psi_\uparrow^* \Psi_\downarrow) \sin(\phi), \\ \langle \sigma_y \rangle &= \text{Re}(\Psi_\uparrow^* \Psi_\downarrow) \sin(\phi) + \text{Im}(\Psi_\uparrow^* \Psi_\downarrow) \cos(\phi). \end{aligned} \quad (10)$$

Since electron spin follows the magnetization, the wave functions are different for Néel and Bloch skyrmions [see Eq. (6)]. For the Bloch-type skyrmion the wave functions have the form

$$\begin{aligned} \Psi_\uparrow(\rho) &= \cos[\theta(\rho)/2], \\ \Psi_\downarrow(\rho) &= -i \sin[\theta(\rho)/2]. \end{aligned} \quad (11)$$

Here θ changes from 0 to π across the DW width w_{dw} in the region $\rho \sim r_{\text{sk}}$.

For the Néel-type skyrmion the wave functions are given by

$$\begin{aligned} \Psi_\uparrow(\rho) &= \cos[\theta(\rho)/2], \\ \Psi_\downarrow(\rho) &= \sin[\theta(\rho)/2]. \end{aligned} \quad (12)$$

The matrix elements of the spin-orbit interaction $H_{\text{so}}(\mathbf{k}) = \langle \Psi | H_{\text{so}} | \Psi \rangle$ have the form

$$\begin{aligned} H_{\text{so}}(\mathbf{k}) &= \int d^3r \Psi_\uparrow^* \Psi_\downarrow (e^{i\phi/2} H_{\text{so}}^+ e^{i\phi/2}) + \Psi_\uparrow \Psi_\downarrow^* (e^{-i\phi/2} H_{\text{so}}^- e^{-i\phi/2}) \\ &\quad + \Psi_\uparrow^* \Psi_\downarrow e^{i\phi} (e^{-i\mathbf{k}\mathbf{r}} H_{\text{so}}^+ e^{i\mathbf{k}\mathbf{r}}) + \Psi_\uparrow \Psi_\downarrow^* e^{-i\phi} (e^{-i\mathbf{k}\mathbf{r}} H_{\text{so}}^- e^{i\mathbf{k}\mathbf{r}}). \end{aligned} \quad (13)$$

The first line describes the action of the SO operator on the spin part of the wave function while the second line describes the action of the SO operator on the coordinate part. To calculate the second line we use the SO operator defined in the Cartesian coordinate [Eq. (4)]. The second line is linear in the quasimomentum \mathbf{k} and leads to zero contribution to the SOI energy after averaging over all electrons. Therefore, we keep only the first two terms in Eq. (13):

$$\begin{aligned} H_{\text{so}}(\mathbf{k}) &= -\alpha_{\text{so}} \hbar \left[\int d^3r \left(\Psi_\uparrow^* \frac{\partial \Psi_\downarrow}{\partial \rho} - \Psi_\downarrow^* \frac{\partial \Psi_\uparrow}{\partial \rho} \right) \right. \\ &\quad \left. + i \text{Im} \int d^3r \frac{\Psi_\downarrow^* \Psi_\uparrow}{\rho} \right]. \end{aligned} \quad (14)$$

In a Sk the magnetization variation happens far from the Sk center around $\rho = r_{\text{sk}}$. Therefore, only electrons near the transition region (Sk DW) give a nonzero contribution to the SOI energy. We assume that the electron localization region is much smaller than the Sk radius r_{sk} and DW width w_{dw} . This assumption is valid for skyrmions in the range of 10 to 100 nm and DW width of order of 10 nm which is much bigger than the electron momentum scattering length.

The integral in Eq. (14) is zero for the Bloch-type skyrmion.

$$H_{\text{so}}^{\text{Bloch}}(\mathbf{k}, \rho) = 0. \quad (15)$$

For the Néel-type skyrmion the SOI contribution is nonzero and negative, decreasing the total system energy. For the Néel-type skyrmions we have

$$H_{\text{so}}^{\text{Néel}}(\mathbf{k}, \rho) = -\alpha_{\text{so}} \hbar \frac{1}{2} \frac{\partial \theta}{\partial \rho}. \quad (16)$$

As one can see, the expression for the SO interaction of a single electron does not depend on the electron momentum \mathbf{k} . Therefore, averaging over all electrons gives a concentration factor. After averaging over the Sk transition region (domain wall) we obtain the total contribution of the SOI for the Néel-type Sk energy

$$H_{\text{so}}^{\text{NéelTot}} = -\alpha_{\text{so}} \pi^2 r_{\text{sk}} t n \hbar, \quad (17)$$

where n is the electron concentration inside of a Sk DW.

Beside the Sk, a few other states may occur in the MO film. These states are either collinear or noncollinear but with fast varying rotation direction. Therefore, these states produce a zero average SOI contribution.

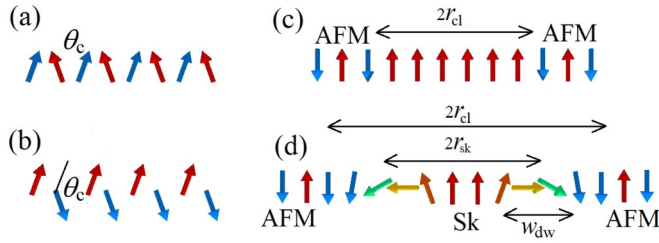


FIG. 2. Magnetic states (cross sections) considered in this work. (a) Canted state of the first type. (b) Canted state of the second type. (c) Cross section of a cylindrically symmetric FM cluster with radius r_{cl} surrounded by the AFM region. (d) Cross section of a cylindrically symmetric cluster with radius r_{cl} surrounded by AFM regions. A Sk with radius r_{sk} and DW thickness w_{dw} is inside the cluster.

III. DIFFERENT MAGNETIC STATES OF THE SYSTEM

In this section we consider three possible magnetic states in the MO film. For all states we assume that magnetization is uniform across the magnetic film thickness. First, we consider the uniform state with canted magnetic moments [see Figs. 2(a) and 2(b)]. We assume that a checkerboard magnetic structure appears in this state [26]. At that neighboring magnetic moments are tilted by the angle θ_c with respect to each other. If $\theta_c = 0$ one has a FM state, while $\theta_c = \pi$ corresponds to an AFM state. Average magnetization in this case has the form $m_{av}^{can} = m_s \cos(\theta_c/2)/\Delta^3$. There are two types of this state: (i) the average magnetization is directed along the z axis (anisotropy axis [see Fig. 2(a)] and (ii) the average magnetization is in the plane of the sample [see Fig. 2(b)]. The first type is realized for large average magnetization (close to FM state). The second type is more favorable for small average magnetization when the system is close to the AFM state. Electron density n_0 in this state is uniform.

The second state is the state with uniformly magnetized FM clusters in an AFM matrix [35] shown in Fig. 2(c). The cluster is cylindrically symmetric (a cut is shown in the figure). This state is characterized by two parameters: (1) the average ratio of FM cluster area S_{cl} to the total sample area S_s , and (2) the average cluster radius r_c . Note that the different FM clusters may have opposite orientation of magnetization. Therefore, we neglect the magnetostatic interaction between them using the fact that the cluster size is much bigger than the film thickness. Below we show that appearance of the cluster state is mostly defined by the competition between exchange and kinetic energy and weakly depends on the magnetostatic energy.

The third state is the one where a Sk stays inside of a cluster. Part of the cluster is magnetized up and part of the cluster is magnetized down [see Fig. 2(d)]. The DW is in between these two parts. Such a system has two more parameters: the skyrmion radius r_{sk} and the DW thickness w_{dw} .

Note that ground magnetic state of the system can be different from the considered three states. In particular, a FM cluster may split into FM domains with opposite magnetization and some nonzero or zero topological charge. Here we are not considering this state. Instead, we study a skyrmion in the FM cluster that is a metastable state of the system. The skyrmion state can be created by a tip of a magnetic force microscope or by other means.

A. OOP anisotropy requirement

While we consider out-of-plane magnetic anisotropy $K > 0$, the magnetostatic interaction can transform it to effectively in-plane anisotropy. In the case of canted uniform state the effective magnetic anisotropy is given by $K_{eff}^{can} = K - 4\pi m_s^2/\Delta^3 \cos(\theta_c/2)$. We assume that $K_{eff}^{can} > 1$ even at $\theta_c = 0$. In this case the effective anisotropy is out-of-plane in all considered magnetic states. Experimental observations of magnetic behavior of several bilayer systems with magnetic oxides evidence that out-of-plane magnetic anisotropy can be realized in practice [12].

B. Uniform canted state

The canted state of the first type is characterized by the canting angle θ_c between neighboring magnetic moments. The SO energy is zero in this case because on average the magnetization rotation is absent [average $\partial\theta/\partial\mathbf{r}$ in Eq. (16) is zero]:

$$E_{so}^{can1} = 0. \quad (18)$$

The MS, anisotropy, exchange, and kinetic average energies are given by the following expressions:

$$\frac{E_{ms}^{can1}}{S_s t} = 2\pi \Omega_{dd} \cos^2(\theta_c/2), \quad (19)$$

$$\frac{E_{an}^{can1}}{S_s t} = -\tilde{K} \cos^2(\theta_c/2) S_s t / 2, \quad (20)$$

$$\frac{E_{ex}^{can1}}{S_s t} \approx -3\tilde{J} \cos(\theta_c), \quad (21)$$

$$\frac{E_k^{can1}}{S_s t} = -2\tilde{t}_0 \cos(\theta_c/2) (4\tilde{n}_0 - 2\pi\tilde{t}\tilde{n}_0^2). \quad (22)$$

Here we introduced normalized quantities $\tilde{t} = t/\Delta$, $\tilde{n}_0 = n_0 * \Delta^3$, $\tilde{t}_0 = t_0/\Delta^3$, $\tilde{K} = K/\Delta^3$, $\tilde{J} = J/\Delta^3$, and $\Omega_{dd} = m_s^2/\Delta^6$. The sample area is denoted S_s .

For the second type of the canted state the kinetic and exchange energies are the same, $E_k^{can1} = E_k^{can2}$ and $E_{ex}^{can1} = E_{ex}^{can2}$. The MS energy is zero, $E_{ms}^{can2} = 0$. And the anisotropy energy has the form

$$\frac{E_{an}^{can2}}{S_s t} = -\tilde{K} \sin^2(\theta_c/2) / 2. \quad (23)$$

Comparing the energies of two canted states and choosing the one that is smaller we obtain the single expression for the canted state energy:

$$\begin{aligned} \frac{E_{tot}^{can}}{S_s t} = & -3\tilde{J} \cos(\theta_c) - 2\tilde{t}_0 \cos(\theta_c/2) (4\tilde{n}_0 - 2\pi\tilde{t}\tilde{n}_0^2) \\ & + \begin{cases} (2\pi\Omega_{dd} - \tilde{K}/2) \cos^2(\frac{\theta_c}{2}), \cos^2(\frac{\theta_c}{2}) > \frac{\tilde{K}}{(\tilde{K} - 4\pi\Omega_{dd})} \\ -\tilde{K}/2 \sin^2(\theta_c/2), \cos^2(\frac{\theta_c}{2}) < \frac{\tilde{K}}{2(\tilde{K}/2 - 2\pi\Omega_{dd})}. \end{cases} \end{aligned} \quad (24)$$

C. State with uniform FM clusters

The uniform cluster state is characterized by the cluster area S_{cl} and cluster size r_{cl} . We assume that the magnetic state in the clusters is the FM one. Outside the clusters there

is an AFM state. At that, all conduction electrons are gathered inside of the clusters. Therefore, the clusters are charged negatively and the AFM regions are charged positively. The contribution due to long-range Coulomb interaction $E_{\text{Coul}}^{\text{cl}}$ becomes finite. In addition, the phase boundary between FM cluster and AFM surrounding space appears introducing the phase boundary energy $E_{\text{pb}}^{\text{cl}}$. The magnetic state is collinear. Therefore, the SOI does not contribute to the system energy. The total cluster energy $E_{\text{tot}}^{\text{cl}}$ has the form

$$E_{\text{tot}}^{\text{cl}} = E_{\text{ex}}^{\text{cl}} + E_{\text{an}}^{\text{cl}} + E_{\text{ms}}^{\text{cl}} + E_{\text{k}}^{\text{cl}} + E_{\text{Coul}}^{\text{cl}} + E_{\text{pb}}^{\text{cl}}. \quad (25)$$

We consider all these contributions in detail. The exchange energy of this state has the form

$$\frac{E_{\text{ex}}^{\text{cl}}}{S_{\text{st}}} \approx 3\tilde{J}(1 - 2\eta). \quad (26)$$

Here we introduce the parameter $\eta = S_{\text{cl}}/S_{\text{s}}$. The anisotropy energy is minimized for this state:

$$\frac{E_{\text{an}}^{\text{cl}}}{S_{\text{st}}} = -\tilde{K}/2. \quad (27)$$

For the FM cluster with cylindrical shape the MS energy can be estimated using a demagnetizing factor $N_{\text{dem}} = 4\pi/(2t/\sqrt{\pi}/r_{\text{cl}} + 1)$ [48]. The cluster MS energy is given by

$$\frac{E_{\text{ms}}^{\text{cl}}}{S_{\text{st}}} = \frac{2\pi\Omega_{\text{dd}}}{\frac{2t}{\sqrt{\pi}r_{\text{cl}}} + 1}. \quad (28)$$

The MS energy can be calculated more precisely using the expression

$$E_{\text{ms}}^{\text{cl}} = \int_{\Omega_{\text{cl}}} \int_{\Omega_{\text{cl}}} E_{\text{dd}}(\mathbf{r}, \mathbf{r}') d^3r d^3r'. \quad (29)$$

The kinetic energy of the FM cluster state has the form

$$\frac{E_{\text{k}}^{\text{cl}}}{S_{\text{st}}} = -2\tilde{t}_0(4\tilde{n}_0 - 2\pi\tilde{t}\tilde{n}_0^2/\eta). \quad (30)$$

The above kinetic energy is written for a parabolic band. Therefore, for $\eta \rightarrow 0$ (AFM uniform state) the kinetic energy in this equation is infinite. For very small clusters the electron density reaches its limiting value 1 electron per site ($\Delta^3 n_0/\eta = 1$) and cannot grow more. At this value the whole electronic band is filled and the total kinetic energy becomes zero. The compression ratio η cannot be smaller than $\Delta^3 n_0$.

The distribution of electron density in this state is inhomogeneous and the long-range Coulomb interaction appears. Clusters are charged negatively with the density $-|e|n_0(1/\eta - 1)$, the space surrounding the cluster is positively charged with the density $|e|n_0$. To simplify, the problem we consider is noninteracting clusters. This assumption is justified because the region including the cluster and surrounding matrix is neutral on average. Therefore, the main contribution to the Coulomb energy appears due to the interaction of a negatively charged cluster with the positively charged surrounding media. To estimate this energy we replace the cluster with an infinitely thin disk with uniform charge. This disk is surrounded by a positively charged ring. The total charge is zero. The disk radius is r_{cl} , and the ring external radius is

$r_{\text{d}} = r_{\text{cl}}/\sqrt{\eta}$. The Coulomb energy has the form

$$\frac{E_{\text{Coul}}^{\text{cl}}}{S_{\text{st}}} = \frac{2e^2}{t(\varepsilon + 1)} \frac{\eta}{\pi r_{\text{cl}}^2} \int_{|\mathbf{r}_1| < R_{\text{d}}} \int_{|\mathbf{r}_2| < R_{\text{d}}} d^2r_1 d^2r_2 \frac{\sigma(r_1)\sigma(r_2)}{|\mathbf{r}_1 - \mathbf{r}_2|}. \quad (31)$$

Here the surface density $\sigma(r) = n_0 t(1/\eta - 1)$ for $r < r_{\text{cl}}$ and $\sigma(r) = -n_0 t$ for $r_{\text{cl}}/\eta > r > r_{\text{cl}}$. The dielectric permittivity in the denominator of Eq. (31) is the substrate dielectric constant. The electric field produced by the charged regions of the MO film penetrates the substrate and interacts with it. Generally, on one side the MO film is surrounded by air with dielectric permittivity of 1 and on the other side there is a substrate with dielectric permittivity ε . Varying the dielectric permittivity of the substrate one can control the strength of the Coulomb interaction.

The last energy contribution is due to the phase boundary. There are two contributions to the phase boundary energy: (1) exchange interaction $E_{\text{pb}}^{\text{ex}} \approx \tilde{J}l_{\text{cl}}t\Delta$, where $l_{\text{cl}} = 2\pi r_{\text{cl}}$ is the cluster phase boundary length. The arrangement of magnetic moments at the cluster boundary is like the following $\dots \uparrow\uparrow\uparrow\downarrow\downarrow\downarrow \dots$. Therefore, the phase boundary exchange energy contribution is negative and favors formation of such a boundary. Anisotropy energy is minimized for collinear magnetic state and does not contribute to the phase boundary energy. Oppositely, the kinetic energy contribution is positive. Electrons have a barrier at the phase boundary leading to the kinetic energy increase. We estimate this contribution as follows. Inside the cluster an electron can jump from its site to all six neighboring sites. Therefore, the energy is proportional to $-3t_0$. At the boundary one of the directions is prohibited. Therefore, the energy increases by $t_0/2$. This gives us an estimate of the kinetic energy increase $E_{\text{pb}}^{\text{kin}} \approx l_{\text{cl}}t\Delta\tilde{t}_0/2(4\tilde{n}_0 - 2\pi\tilde{t}\tilde{n}_0/\eta)$. The total phase boundary energy is given by $E_{\text{pb}} \approx l_{\text{cl}}t\Delta[\tilde{J} + \tilde{t}_0/2(4\tilde{n}_0 - 2\pi\tilde{t}\tilde{n}_0/\eta)]$. Finally, for multiple clusters we obtain the following average phase boundary energy:

$$\frac{E_{\text{pb}}^{\text{cl}}}{S_{\text{st}}} = \frac{2\eta\Delta}{r_{\text{cl}}} [\tilde{J} + \tilde{t}_0/2(4\tilde{n}_0 - 2\pi\tilde{t}\tilde{n}_0/\eta)]. \quad (32)$$

Minimizing the energy over η and r_{cl} one can find the relative clusters area and size. Exchange, anisotropy, and kinetic energies in Eqs. (26), (27), and (30) do not depend on the cluster size r_{c} . Therefore, the cluster size (at fixed clusters area S_{cl}) is defined by the competition of the Coulomb interaction, MS interaction, and the phase boundary energy. Our estimates show that the MS energy can be neglected when we define the cluster size and average cluster area for typical magnetization of MOs. The Coulomb energy decreases the cluster size since it prefers to have short-range charge inhomogeneities rather than the long-range ones. In contrast, the phase boundary increases the cluster size.

D. Appearance of the FM cluster

The system is described by several parameters: J , t_0 , K , Ω_{dd} , t , n_0 , and ε . We can reduce the number of independent parameters. First, we introduce the effective anisotropy $\tilde{K}_{\text{eff}} = K - 4\pi\Omega_{\text{dd}}$. Such a combination enters most of the equations above. Also, we normalize all energies by \tilde{t}_0 . Finally,

we obtain five independent parameters: $J_{\text{eff}} = \tilde{J}/\tilde{t}_0$, $K_{\text{eff}} = \tilde{K}_{\text{eff}}/\tilde{t}_0$, \tilde{n}_0 , \tilde{t} , and ε . Below we fix the film thickness $\tilde{t} = 2.5$ (film thickness is approximately 1 nm) and discuss the system properties using 2D state diagrams in coordinates $(\tilde{n}_0, J_{\text{eff}})$ for several values of substrate dielectric constant ε . We find that the effective anisotropy does not qualitatively change the state diagrams. Therefore, we show phase diagrams for $K_{\text{eff}} = 0.002$ only.

We use parameters which correspond to real materials. In particular, we consider $0.01 < J_{\text{eff}} < 0.05$. Based on the analysis of magnetic ordering temperatures of the magnetic oxides (such as LaSrMnO) in the range 100–300 K (following Ref. [16]) we get J of about $0.03t_0$. The characteristic kinetic energy in MO is in the range of tens of meV to hundreds of meV. Magnetization of the LSMO material (in the LSMO/SRO bilayer) is about $M_s = 350$ G ($5/2 \mu_B$ per unit cell with 0.4 nm size). Using this value we find that the MS contribution to energy is negligible. For $t_0 = 100$ meV, the magnetic anisotropy value $K_{\text{eff}} = 0.002$ corresponds to the anisotropy energy density of 500 kJ/m³, which is typical for magnetic oxides [12,16]. The concentration of conduction electrons is usually controlled by doping in MOs. Here we study the region of low doping 0.001–0.06 electrons per unit cell. In this region the correlation effects are weak.

Note that due to the interfacial effect the actual doping level may be different and should be defined experimentally. For the dielectric constant we compare two different values $\varepsilon = 50$ and $\varepsilon = 2000$. As we mentioned in the Introduction the DMI was observed in LSMO/SRO bilayer films. So, this is a suitable pair of material (with right doping level) to study effects discussed in the present work. Many oxide materials have a dielectric constant of several tens (like TiO₂ or La₂O₃) [49]. A lot of ferroelectrics have a dielectric constant of a few thousand [50]. In most ferroelectrics, the dielectric constant can be tuned by electric field or by varying temperature [50]. In some organic ferroelectrics the dielectric constant may change with temperature from below ten to a few thousand [51]. Thus, one can control the Coulomb energy using external parameters and eventually control the magnetic state of the system, see Ref. [42].

First, we investigate where the cluster state is more favorable than the canted state. To do this for each set of parameters $(\tilde{n}_0, J_{\text{eff}})$ we minimize the cluster state energy $E_{\text{tot}}^{\text{cl}}$ [Eq. (25)] over the relative cluster area η and the cluster radius r_{cl} and the canted state energy $E_{\text{tot}}^{\text{can}}$ [Eq. (24)] over the canting angle θ_c . Then we compare the optimized cluster state and canted state energies and choose the lowest one.

Figure 3 shows the diagram comparing canted state and the FM cluster state for $K_{\text{eff}} = 0.002$ and $\varepsilon = 2000$. Blue areas in the upper and lower right corners show the parameters region where the canted state is more favorable. In the rest of the parameter space (the colored region) the FM cluster state is more favorable. Color in this region indicates the relative clusters area η . The relative cluster area η grows as one increases the electron concentration. This can be understood as follows. The electrons mediate an effective FM interaction between localized magnetic moments. Therefore, increasing the electron number leads to formation of a bigger FM region in the film. The cluster size also increases as one decreases the direct AFM interaction.

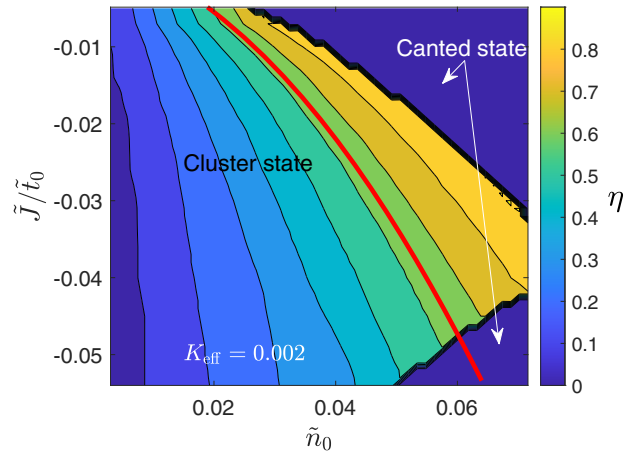


FIG. 3. State diagram for MO film. All parameters defined in the text. Color shows the value of compression ratio for cluster state η . Small blue region in the right bottom corner corresponds to a canted state. The red line shows the percolation threshold with $\eta = 0.65$. Above this line the percolation appears and no separate clusters exist.

Note that as the relative cluster area grows the representation of the system as an ensemble of FM clusters becomes less relevant. For a certain cluster area percolation appears and an infinite cluster spanning the whole sample forms. Such a film cannot be described in terms of clusters. Therefore, we do not consider such a state as cluster state in this work. The percolation threshold for 2D film is $\eta = 0.65$. The threshold is shown by the red line in Fig. 3. Only the state to the right of this line is considered as a cluster state.

Increasing K_{eff} one can increase the parameters region with the cluster state because anisotropy favors FM or AFM state and not the canted one.

Cluster size is defined by the competition of the long-range Coulomb energy and the cluster boundary energy. The Coulomb interaction makes the cluster size smaller, while the cluster boundary energy grows with reducing the cluster size. Figure 4 shows the optimum cluster radius for the same parameters as in Fig. 3 ($K_{\text{eff}} = 0.002$, $\varepsilon = 2000$). Comparing Figs. 4 and 3 one can see that the cluster radius decreases with increasing the compression ratio $1/\eta$. This happens because the increase of the compression ratio increases the charge inhomogeneity and therefore the long-range Coulomb interaction leading to the cluster size reduction. At low electron concentration and large exchange constant the cluster radius becomes very small (1 nm). This region is generally beyond the validity of our model. Such small clusters cannot host skyrmions. The skyrmion size is restricted by the DW width. The skyrmion radius should be bigger than two DW thicknesses. The DW thickness is a few nm. Therefore, clusters with radius less than 5 nm cannot have skyrmions. We show a 5 nm cluster radius by the orange line in Fig. 4. Finally, the region of parameters interesting for skyrmion formation is restricted by the percolation limit on one side (red line) and the smallest possible cluster radius (orange line).

The substrate dielectric constant is important. Figures 3 and 4 show the case of high dielectric constant, $\varepsilon = 2000$. Figures 5 and 6 show the state diagram for low dielectric constant $\varepsilon = 50$. In this case the Coulomb interaction is strong.

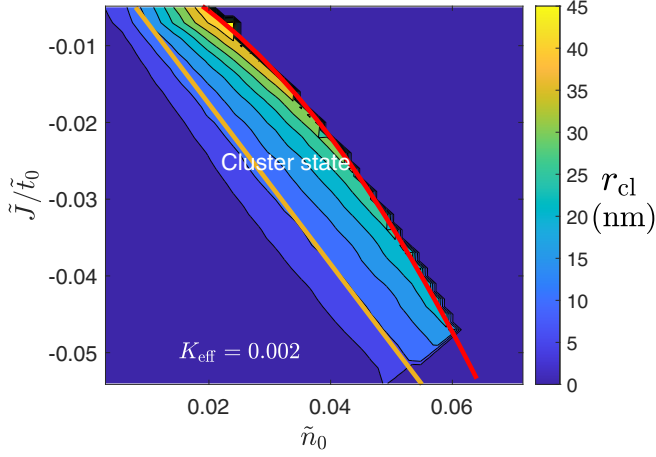


FIG. 4. Cluster radius in MO film vs electron concentration n_0 and the normalized direct exchange interaction constant \tilde{J}/\tilde{t}_0 . All parameters are defined in the text. The red line shows the percolation threshold where $\eta = 0.65$. Above this line the percolation appears and no separate clusters exist. Orange line shows the cluster radius of 5 nm.

It does not change the region of parameters where the phase separation appears. However, it reduces the clusters size in the phase separated state. Big clusters which can host skyrmions appear in a very small parameters region (enclosed by the red and orange lines in Fig. 6).

E. Cluster with a skyrmion

Consider a FM cluster with the radius r_c in an AFM matrix. Let the cluster contain the Néel skyrmion with radius r_{sk} . The skyrmion consists of three regions [see Fig. 2(d)]. The inner FM part, the DW, and the outer FM part with opposite magnetization. The Sk radius r_{sk} is assumed to be much bigger than the DW width w_{dw} . The DW contains approximately

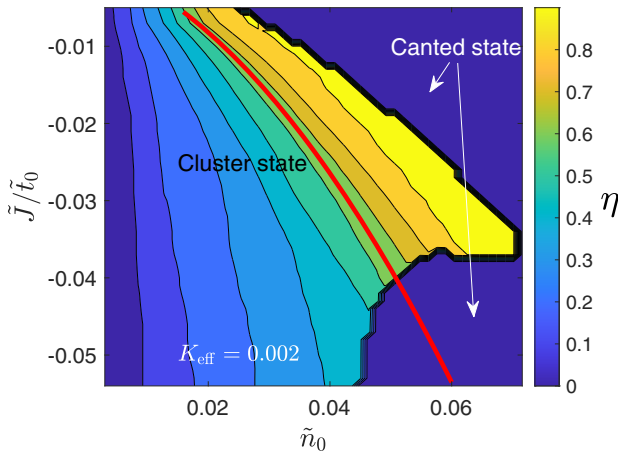


FIG. 5. Diagram of states for the MO film on the substrate with $\varepsilon = 50$. See parameters in the text. Color shows the compression ratio value for cluster state η . Small blue region in the right bottom corner is where the canted state is more favorable. The red line shows where $\eta = 0.65$. This line shows the percolation threshold. Above this line the percolation appears and no separate clusters are possible.

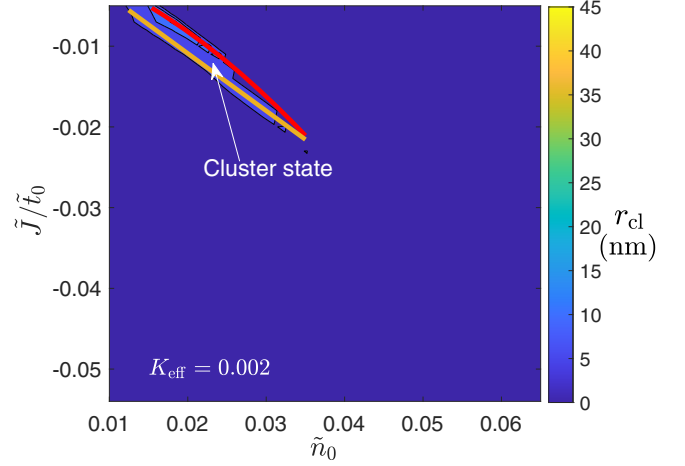


FIG. 6. Cluster radius in MO film on the substrate with $\varepsilon = 50$ as a function of electron concentration n_0 and the normalized direct exchange interaction constant \tilde{J}/\tilde{t}_0 . See parameters in the text. The red line shows the percolation threshold where $\eta = 0.65$. Above this line the percolation appears and no separate clusters are possible. Orange line shows the cluster radius of 5 nm.

$N_{dw} = w_{dw}/\Delta$ atomic planes. The magnetization rotates in the DW. The angle between the magnetic moments in the neighboring atomic plane can be estimated as $\Delta\theta = \pi/N_{dw}$. Note that the DW in the skyrmion is curved. Therefore, if one moves along the DW the magnetization orientation also rotates. Full 2π rotation occurs along the DW length $2\pi r_{sk}$. One can estimate the mutual angle between two neighboring magnetic moments in the same DW plane as $\Delta\theta_{||} = \Delta/r_{sk}$.

The Sk state energy differs from the FM cluster energy by the DW energy. The energy of the DW consists of four parts: (1) the exchange energy; (2) the anisotropy energy; (3) the kinetic energy of electrons; and (4) the spin-orbit interaction of electrons. The exchange component has the form

$$\begin{aligned} \Delta W_{dw}^{ex} &= |J|N_{dw}S_{dw}[\cos(\Delta\theta) - 1 + \cos(\Delta\theta_{||}) - 1] \\ &\approx -\frac{|J|t\pi}{\Delta} \left(\frac{r_{sk}\pi^2}{w_{dw}} + \frac{w_{dw}}{r_{sk}} \right). \end{aligned} \quad (33)$$

Here S_{dw} is the number of magnetic moments along the DW area. It can be estimated as $S_{dw} = 2\pi r_{sk}t/\Delta^2$. For the magnetic anisotropy energy we obtain

$$\Delta W_{dw}^{an} = \frac{KN_{dw}S_{dw}}{4} = \frac{\pi Kr_{sk}tw_{dw}}{4\Delta^3}. \quad (34)$$

The total kinetic energy of all electrons in the DW region has the form

$$\begin{aligned} W_{dw}^{kin} &= -2\pi r_{sk}w_{dw}t t_0(4n - 2\pi\Delta^2tn^2) \\ &\quad \times [\cos(\Delta\theta/2) + \cos(\Delta\theta_{||}/2)]. \end{aligned} \quad (35)$$

So, the DW contribution to the total kinetic energy is given by

$$\Delta W_{dw}^{kin} = \pi t t_0 \Delta^2 (n - \pi \Delta^2 t n^2 / 2) \left(\frac{r_{sk} \pi^2}{w_{dw}} + \frac{w_{dw}}{r_{sk}} \right). \quad (36)$$

Note that all three above contributions do not depend on the DW type and are the same for both Néel and Bloch DWs. The only assumption made is that within the DW the spins are

rotated in the same plane by the same angle as we go from one plane to the next one.

The next contribution to the cluster energy is the SOI. According to Eq. (17) the SOI energy for the Néel Sk has the form

$$\Delta W_{\text{dw}}^{\text{so}} = -\alpha_{\text{so}} \hbar \pi^2 r_{\text{sk}} t n_{\text{dw}}. \quad (37)$$

Beside the DW energy, the existence of two oppositely magnetized regions of the cluster changes the magneto-static energy of the system (comparing to the state with FM clusters). The correction to the dipole-dipole energy due to skyrmion formation can be numerically calculated using Eq. (3) with Sk magnetization distribution. We denote the difference between the FM state MS energy and the Sk state MS energy as $\Delta W_{\text{ms}}^{\text{sk}}$.

The total skyrmion energy (energy difference between FM and Sk states) is a sum of all considered contributions:

$$\Delta W_{\text{Sk}}^{\text{tot}} = \Delta W_{\text{dw}}^{\text{ex}} + \Delta W_{\text{dw}}^{\text{an}} + W_{\text{dw}}^{\text{kin}} + \Delta W_{\text{dw}}^{\text{so}} + \Delta W_{\text{Sk}}^{\text{ms}}. \quad (38)$$

F. Skyrmion stability diagram

Formation of skyrmions depends on competition of different energy contributions considered above. A skyrmion can be considered as a cylindrical DW. The kinetic energy of an electron favors the FM order of magnetic moments in the cluster, the AFM direct exchange counteracts this. In total, in the parameters region where clusters form, the kinetic energy dominates producing the effective exchange interaction of FM type, which counteracts the DW formation. Magnetic anisotropy also increases the DW energy. The magnetostatic interaction favors formation of magnetic domains and therefore favors formation of skyrmion even in the absence of SOI (DMI interaction). However, our calculations show that the MS energy in such a thin film with typical magnetization of the MOs produces a very low energy contribution and is not important. Similar estimates can be found in other papers [52–54]. The SOI of electrons leads to effective DMI interaction, reducing the energy of a DW in the cluster. If DW energy is positive the Sk does not exist. But for large enough DMI interaction the DW energy becomes negative and skyrmion formation is possible. Note that in this case the length of the DW grows but it is limited by the size of the cluster. Thus, the skyrmion formed in the cluster has a radius close to the cluster size. Our simulations show that it is smaller due to cluster boundary effect, DW thickness, and the MS interaction.

Figure 7 shows the state diagram in coordinates \tilde{J} , \tilde{n}_0 ($\varepsilon = 2000$, $K_{\text{eff}} = 0.002$, $\alpha_{\text{so}} \hbar / \Delta = 0.05 t_0$) where the region with Sk formation in the cluster is shown. The blue region corresponds to the case where clusters are absent or the Sk is unstable in the cluster. The colored region shows the Sk radius in the skyrmion stability region. Generally, the Sk is stable in the part of the region shown in Fig. 4 between orange and red lines and at high enough \tilde{J} . The smaller the direct AFM exchange coupling constant, the bigger the effective total FM exchange interaction and therefore the bigger the DW energy. Thus, at low \tilde{J} the skyrmion formation is less possible. This is why the skyrmion stability regions correspond to high values of \tilde{J} .

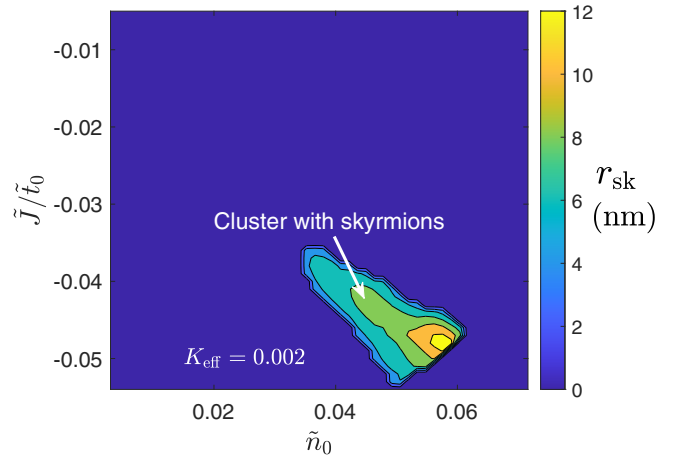


FIG. 7. State diagram of MO film placed on top of a substrate with $\varepsilon = 2000$. All parameters are the same as in Fig. 3. Color shows the skyrmion radius in the parameters region where skyrmion is stable. Blue color shows the parameter region with an unstable skyrmion.

Colors show the Sk radius. Comparing Figs. 7 and 4 one can see that the Sk radius is almost the same as the cluster radius.

In the skyrmion stability region the topological charge of the cluster is one.

For small substrate dielectric constant ($\varepsilon = 50$) the skyrmion is unstable in the considered parameter region. This is because at low ε , big enough clusters occur only for small exchange interaction constant \tilde{J} [see Fig. 5(b)]. In this region the DW energy is positive preventing formation of skyrmion.

As we mention above, in some substrates the dielectric constant can be controlled using electric field or temperature. In particular, this can be done in ferroelectric materials. This opens the way to manipulate skyrmions in a hybrid structure with MO film on top of a ferroelectric substrate.

G. Cluster electric charge

Above, we mentioned that electron concentration inside of clusters is bigger than outside of clusters. Therefore, the electric charge occurs in the cluster. Depending on the compression ratio and the cluster size the total electric charge can be different. A number of excessive electrons is given by

$$N_{\text{el}} = \pi r_{\text{cl}}^2 (1/\eta - 1) n_0. \quad (39)$$

Figure 8 shows the dependence of the cluster charge (N_{el}) on the system parameters. While even the cluster without the Sk has a nonzero charge, we show here only the region with stable Sk. In this region clusters have both topological and electrical charges. Generally, the bigger the cluster size the bigger the electric charge it has. For a cluster radius of 12 nm, the number of excessive electrons reaches 600 meaning that such a cluster is sensitive to the electric field. Applying an electric field one can move the cluster and move the Sk. One can consider this as a magnetoelectric phenomena, where one can move magnetic Sk with an electric field. Such an electric field can be created with a scanning probe microscope tip or with applying a voltage along the MO film. Due to

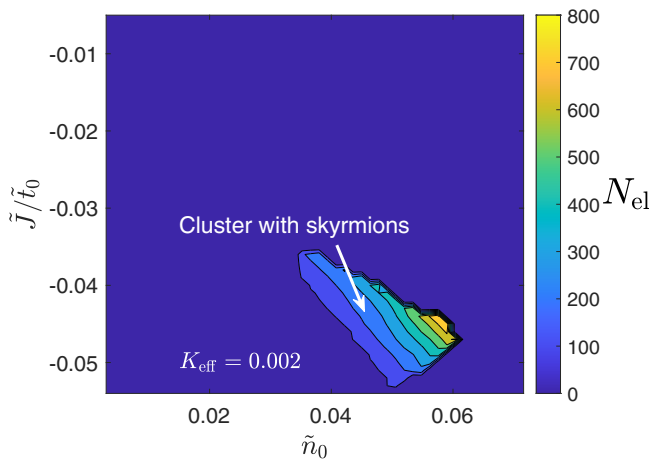


FIG. 8. Diagram of states for the MO film placed on top of a substrate with $\varepsilon = 2000$. Other parameters are the same as in Fig. 3. Color shows a number of excessive electrons inside a cluster in the parameters region where the skyrmion is stable. Blue color denotes the parameter region where the skyrmion is not stable.

a big cluster charge the electric field needed to move the cluster and Sk can be much lower than the field (and current) needed to move Sk in artificial Co/Pt multilayer structures via spin-transfer torque or spin-orbit torque effects.

H. Comments on thermal stability of skyrmions in MO

We consider the system at zero temperature and do not take thermal fluctuations into account. Thermal stability of skyrmions attracted a lot of attention recently [55,56]. There are two paths for the skyrmion to annihilate due to the thermal fluctuations: (1) through the contraction of skyrmion size and finally collapsing the skyrmion and (2) annihilation through the boundary of a laterally confined magnetic structure. The first path is energy consuming since the thermal fluctuations

need to overcome exchange interaction in this case. The second scenario requires less energy and therefore is the more probable one. Note however, that laterally confined magnetic film considered in previous papers is not the same as the laterally confined magnetic cluster in the AFM matrix considered in our paper. The boundary between FM and AFM region may move and deform. So, the skyrmion annihilation conditions may be very different and requires further studying.

IV. CONCLUSION

We considered an ultrathin magnetic oxide film on top of the high dielectric constant substrate. We used the double exchange model to describe the system behavior. We include the Rashba spin-orbit interaction in the model. This interaction exists at the interface of the magnetic oxide and the substrate or other additional layer. The Rashba spin-orbit interaction acts on electrons and is transformed into an effective Dzyaloshinskii-Moriya interaction for localized magnetic moments in the magnetic oxide film. We showed that the phase separation appears in such a magnetic oxide film in a certain parameters region. Due to the phase separation electrically charged magnetic clusters appear. Additionally, the DMI interaction leads to formation of a magnetic skyrmion in the electrically charged clusters. We showed that one can obtain clusters having both electric and topological charges. Importantly, the clusters with sizes suitable for skyrmions formation may occur only for substrates with a high dielectric constant. Otherwise, clusters are too small for a skyrmion appearance.

ACKNOWLEDGMENTS

This research was supported by NSF under Cooperative Agreement Award EEC-1160504. O.G.U. thanks the support of the Russian Ministry of Education and Science under grant 0030-2021-0021.

- [1] C. Moreau-Luchaire, C. Moutafis, N. Reyren, J. Sampaio, C. A. F. Vaz, N. V. Horne, K. Bouzehouane, K. Garcia, C. Deranlot, P. Warnicke, P. Wohlhüter, J.-M. George, M. Weigand, J. Raabe, V. Cros, and A. Fert, *Nat. Nanotechnol.* **11**, 444 (2016).
- [2] W. Legrand, J.-Y. Chauleau, D. Maccariello, N. Reyren, S. Collin, K. Bouzehouane, N. Jaouen, V. Cros, and A. Fert, *Sci. Adv.* **4**, eaat0415 (2018).
- [3] A. Soumyanarayanan, A. L. G. O. M. Raju, A. K. C. Tan, M.-Y. Im, A. P. Petrović, P. Ho, K. H. Khoo, M. Tran, C. K. Gan, F. Ernult, and C. Panagopoulos, *Nat. Mater.* **16**, 898 (2017).
- [4] A. Hrabec, N. A. Porter, A. Wells, M. J. Benitez, G. Burnell, S. McVitie, D. McGrouther, T. A. Moore, and C. H. Marrows, *Phys. Rev. B* **90**, 020402(R) (2014).
- [5] N. S. Gusev, A. V. Sadovnikov, S. A. Nikitov, M. V. Sapozhnikov, and O. G. Udalov, *Phys. Rev. Lett.* **124**, 157202 (2020).
- [6] R. Lavrijsen, D. M. F. Hartmann, A. van den Brink, Y. Yin, B. Barcones, R. A. Duine, M. A. Verheijen, H. J. M. Swagten, and B. Koopmans, *Phys. Rev. B* **91**, 104414 (2015).
- [7] N. K. Duong, M. Raju, A. P. Petrović, R. Tomasello, G. Finocchio, and C. Panagopoulos, *Appl. Phys. Lett.* **114**, 072401 (2019).
- [8] L. Wang, C. Liu, N. Mehmood, G. Han, Y. Wang, X. Xu, C. Feng, Z. Hou, Y. Peng, X. Gao, and G. Yu, *ACS Appl. Mater. Interfaces* **11**, 12098 (2019).
- [9] M. He, G. Li, Z. Zhu, Y. Zhang, L. Peng, R. Li, J. Li, H. Wei, T. Zhao, X.-G. Zhang, S. Wang, S.-Z. Lin, L. Gu, G. Yu, J. W. Cai, and B.-g. Shen, *Phys. Rev. B* **97**, 174419 (2018).
- [10] L. Wang, Q. Feng, Y. Kim, R. Kim, K. H. Lee, S. D. Pollard, Y. J. Shin, H. Zhou, W. Peng, D. Lee, W. Meng, H. Yang, J. H. Han, M. Kim, Q. Lu, and T. W. Noh, *Nat. Mater.* **17**, 1087 (2018).
- [11] L. Caretta, E. Rosenberg, F. Büttner, T. Fakhru, P. Gargiani, M. Valvidares, Z. Chen, P. Reddy, D. A. Muller, C. A. Ross, and G. S. Beach, *Nat. Commun.* **11**, 1090 (2020).
- [12] K.-Y. Meng, A. S. Ahmed, M. Baćani, A.-O. Mandru, X. Zhao, N. Bagués, B. D. Esser, J. Flores, D. W. McComb, H. J. Hug, and F. Yang, *Nano Lett.* **19**, 3169 (2019).
- [13] Y. Li, L. Zhang, Q. Zhang, C. Li, T. Yang, Y. Deng, L. Gu, and D. Wu, *ACS Appl. Mater. Interfaces* **11**, 21268 (2019).

- [14] D. J. Groenendijk, C. Autieri, T. C. van Thiel, W. Brzezicki, J. R. Hortensius, D. Afanasiev, N. Gauquelin, P. Barone, K. H. W. van den Bos, S. van Aert, J. Verbeeck, A. Filippetti, S. Picozzi, M. Cuoco, and A. D. Caviglia, *Phys. Rev. Res.* **2**, 023404 (2020).
- [15] G. Malsch, D. Ivaneyko, P. Milde, L. Wysocki, L. Yang, P. H. M. van Loosdrecht, I. Lindfors-Vrejoiu, and L. M. Eng, *ACS Applied Nano Materials* **3**, 1182 (2020).
- [16] N. Mohanta, E. Dagotto, and S. Okamoto, *Phys. Rev. B* **100**, 064429 (2019).
- [17] L. Yang, L. Wysocki, J. Schopf, L. Jin, A. Kovacs, F. Gunkel, R. Dittmann, Paul H. M. van Loosdrecht, and I. Lindfors-Vrejoiu, *Phys. Rev. Mater.* **5**, 014403 (2021).
- [18] Z. Li, X. Liu, J. Jiang, W. Mi, and H. Bai, *ACS Appl. Electron. Mater.* **2**, 2591 (2020).
- [19] S. Esser, J. Wu, S. Esser, R. Gruhl, A. Jesche, V. Roddatis, V. Moshnyaga, R. Pentcheva, and P. Gegenwart, *Phys. Rev. B* **103**, 214430 (2021).
- [20] M. Ziese, F. Bern, P. D. Esquinazi, and I. Lindfors-Vrejoiu, *Physica Status Solidi (b)* **257**, 1900628 (2020).
- [21] X. Yao, C. Wang, E.-J. Guo, X. Wang, X. Li, L. Liao, Y. Zhou, S. Lin, Q. Jin, C. Ge, M. He, X. Bai, P. Gao, G. Yang, and K.-j. Jin, *ACS Appl. Mater. Interfaces* **14**, 6194 (2022).
- [22] Y. Ohuchi, J. Matsuno, N. Ogawa, Y. Kozuka, M. Uchida, Y. Tokura, and M. Kawasaki, *Nat. Commun.* **9**, 213 (2018).
- [23] S. Chakraverty, T. Matsuda, H. Wadati, J. Okamoto, Y. Yamasaki, H. Nakao, Y. Murakami, S. Ishiwata, M. Kawasaki, Y. Taguchi, Y. Tokura, and H. Y. Hwang, *Phys. Rev. B* **88**, 220405(R) (2013).
- [24] K. Ahadi, L. Galletti, and S. Stemmer, *Appl. Phys. Lett.* **111**, 172403 (2017).
- [25] C. P. Adams, J. W. Lynn, Y. M. Mukovskii, A. A. Arsenov, and D. A. Shulyatev, *Phys. Rev. Lett.* **85**, 3954 (2000).
- [26] J. van den Brink and D. Khomskii, *Phys. Rev. Lett.* **82**, 1016 (1999).
- [27] S. M. Dunaevskii, *Phys. Solid State* **46**, 193 (2004).
- [28] M. B. Salamon and M. Jaime, *Rev. Mod. Phys.* **73**, 583 (2001).
- [29] A. P. Ramirez, *J. Phys.: Condens. Matter* **9**, 8171 (1997).
- [30] S. Weber, P. Lunkenheimer, R. Fichtl, J. Hemberger, V. Tsurkan, and A. Loidl, *Phys. Rev. Lett.* **96**, 157202 (2006).
- [31] E. Nagaev, *Phys. Rep.* **346**, 387 (2001).
- [32] M. Yu. Kagan, D. I. Khomskii, and M. V. Mostovoy, *Eur. Phys. J. B* **12**, 217 (1999).
- [33] K. I. Kugel, A. L. Rakhmanov, A. O. Sboychakov, and D. I. Khomskii, *Phys. Rev. B* **78**, 155113 (2008).
- [34] M. Y. Kagan, A. V. Klaptsov, I. V. Brodsky, K. I. Kugel, A. O. Sboychakov, and A. L. Rakhmanov, *J. Phys. A: Math. Gen.* **36**, 9155 (2003).
- [35] M. Y. Kagan and K. I. Kugel', *Phys. Usp.* **44**, 553 (2001).
- [36] E. Dagotto, T. Hotta, and A. Moreo, *Phys. Rep.* **344**, 1 (2001).
- [37] E. Dagotto, *New J. Phys.* **7**, 67 (2005).
- [38] J. van den Brink, G. Khaliullin, and D. Khomskii, *Phys. Rev. Lett.* **83**, 5118 (1999).
- [39] R. J. Goff and J. P. Attfield, *Phys. Rev. B* **70**, 140404(R) (2004).
- [40] R. Yu, S. Yunoki, S. Dong, and E. Dagotto, *Phys. Rev. B* **80**, 125115 (2009).
- [41] S. Dong, X. Zhang, R. Yu, J.-M. Liu, and E. Dagotto, *Phys. Rev. B* **84**, 155117 (2011).
- [42] O. G. Udalov and I. S. Beloborodov, *Phys. Rev. B* **101**, 174433 (2020).
- [43] O. G. Udalov and I. S. Beloborodov, *Phys. Rev. B* **100**, 155102 (2019).
- [44] S. Banerjee, J. Rowland, O. Erten, and M. Randeria, *Phys. Rev. X* **4**, 031045 (2014).
- [45] S. Banerjee, O. Erten, and M. Randeria, *Nat. Phys.* **9**, 626 (2013).
- [46] G. A. Meza and J. A. Riera, *Phys. Rev. B* **90**, 085107 (2014).
- [47] A. Stern, *Phys. Rev. Lett.* **68**, 1022 (1992).
- [48] M. Sato and Y. Ishii, *J. Appl. Phys.* **66**, 983 (1989).
- [49] J. Robertson, *Rep. Prog. Phys.* **69**, 327 (2006).
- [50] K. M. Johnson, *J. Appl. Phys.* **33**, 2826 (1962).
- [51] G. Giovannetti, S. Kumar, A. Stroppa, J. van den Brink, and S. Picozzi, *Phys. Rev. Lett.* **103**, 266401 (2009).
- [52] N. Vidal-Silva, A. Riveros, and J. Escrig, *J. Magn. Magn. Mater.* **443**, 116 (2017).
- [53] Y. Y. Dai, H. Wang, P. Tao, T. Yang, W. J. Ren, and Z. D. Zhang, *Phys. Rev. B* **88**, 054403 (2013).
- [54] S. Rohart and A. Thiaville, *Phys. Rev. B* **88**, 184422 (2013).
- [55] D. Cortés-Ortuño, W. Wang, M. Beg, R. A. Pepper, M.-A. Bisotti, R. Carey, M. Vowsden, T. Kluyver, O. Hovorka, and H. Fangohr, *Sci. Rep.* **7**, 4060 (2017).
- [56] V. M. Uzdin, M. N. Potkina, I. S. Lobanov, P. F. Bessarab, and H. Jónsson, *Phys. B: Condens. Matter* **549**, 6 (2018), 11th International Symposium on Hysteresis Modeling and Micromagnetics (HMM 2017).